Carbon species solvated in molten carbonate electrolyser cell from first-principles simulations

Antoine Carof [a,1], François-Xavier Coudert [b], Dario Corradini [a,2], Dominika Lesnicki [b,3], Elsa Desmaele [a], Rodolphe Vuilleumier [a,*]

[a] PASTEUR, Département de Chimie, École Normale Supérieure, PSL University, Sorbonne Université, CNRS, 75005, Paris, France
[b] Chimie ParisTech, PSL University, CNRS, Institut de Recherche de Chimie Paris, 75005, Paris, France

HIGHLIGHTS

- Solvation was studied by molecular simulation in molten carbonate used in MCEC/MCFC.
- CO_2 solvated in $LiKCO_3$ at P = 1 atm reacts with CO_3^{2-} to form the transient $C_2O_5^{2-}$.
- $C_2O_4^{2-}$ is also stable while CO interacts weakly with the melt and diffuses quickly.
- O^{2-} forms a flexible complex with four Li^+ in $LiKCO_3$.
- Li^+ and K^+ display different behaviours around charged and neutral solvated species.

ARTICLE INFO

ABSTRACT

We study the solvation of molecules and ions that are key in the context of molten carbonate electrolyser cells using first-principles simulations. Focusing on the electro-reduction of CO_2 to CO in a molten carbonate medium, we investigate the solvation of both the reactant CO_2 and the product CO in the eutectic $LiKCO_3$ (containing 62% Li_2CO_3, 38% K_2CO_3). CO_2 is found to spontaneously react with the carbonate ions to form the transient pyrocarbonate species, $C_2O_5^{2-}$. To investigate the similar reaction that could occur with CO and CO_3^{2-} to form an oxalate, we simulated that species and found it to be stable in the melt, supporting this hypothesis. We further present the solvation of O^{2-}, finding that it shows preferential formation of a complex with four lithium cations. Estimates of the diffusion coefficients of these species are then reported, showing that CO has the faster diffusion of all the molecules and ions studied.

© 2020 Hydrogen Energy Publications LLC. Published by Elsevier Ltd. All rights reserved.

Introduction

Molten carbonates are nowadays used in many applications [1]. For instance, molten carbonate fuel cells (MCFC) can produce electricity in the MW range with long term stability [2]. Moreover, because MCFC consume CO_2 at the cathode side and release CO_2 at the anode side, they have been proposed to combine this electricity production capability with the capture and the concentration of CO_2 out of exhaust gas from

steel mills [3–5]. Alternatively, the high solubility of CO_2 in molten carbonates is a possible path to perform carbon capture and utilization (CCU) by electroreduction of CO_2 in molten carbonate electrolyser cells (MCEC) [6–10]. The reduction of CO_2 in MCEC into amorphous carbon has been well documented and the conversion of CO_2 to CO or even CH_4 has also been evidenced recently [11–13], thus adding another opportunity for carbon capture and utilization using carbonate melts.

Optimizing the conditions for an efficient electroreduction of CO_2 in MCEC, for example by tuning the melt temperature or the composition, calls for a better understanding of the microscopic processes involved. In particular, there is need to better understand the speciation of the carbon species and their solvation properties in the melt. Cyclic voltametry [12] has shown that the mechanism of electroreduction of CO_2 into CO is complex and involves the formation of several other species during the reaction. However, the exact nature of these species remains unclear and cyclic voltametry provides only limited microscopic information about these species.

Several recent studies have highlighted the power of computational approaches for the understanding of these complex systems, and a number of molecular dynamics simulation of molten carbonates have been reported [14–20]. Molecular dynamics simulations can provide a picture of molecular mechanisms and can accurately predict physico-chemical properties, especially in high temperature and high pressure conditions where experiments are hard to perform.

Molecular dynamics simulations exist in two different flavours: first-principles molecular dynamics (FPMD) and force field based molecular dynamics (FFMD). In the latter, energy and nuclear forces are calculated at each time step *via* a force field function. This method is very efficient numerically and can be used to perform molecular dynamics simulation in large systems, but it requires the design and parametrization of a specific force field describing the interactions between the molecular components of the system. On the other hand, FPMD provides an alternative route by computing on the fly the forces acting on the atoms using an explicit description of the electrons *via* quantum chemistry methods (*e.g.* DFT) [21]. FPMD simulations are thus free of force field parametrization and have the further advantage of being able to directly describe chemical phenomena (*e.g.* bond breaking and forming); however they have a much higher computational cost than classical methods. In the context of modelling molten carbonate, FPMD simulations showed in particular that the solvation of CO_2 within $CaCO_3$ at geological conditions (T = 1773 K and GPa pressure) leads to the formation of a transient species, the pyrocarbonate anion $C_2O_5^{2-}$ [15]. This reactivity of CO_2 with the carbonate ions has consequences both on the solubility of CO_2 and on its transport properties; it could not have been observed in a force field-based simulation. FPMD simulations can also be used in combination with FFMD simulations by building new force fields based on the data obtained during the FPMD simulation, and then rely on the efficiency of FFMD to study large systems. This strategy has been successfully applied to the description of alkaline-earth molten carbonates and molten carbonates of lithium, sodium and potassium [16,19,20], for instance in

order to predict the equation of state of liquid $CaCO_3$, its viscosity and its conductivity [14] in good agreement with available experiments [22]. However, these first-principles based FFMD do not allow to study the reactivity and the formation/disproportionation of the transient pyrocarbonate anion in $CaCO_3$, underlining the necessity to use FPMD to model the solvation of potentially reactive species such as CO_2 or CO in molten carbonates.

We present here a FPMD study of the solvation of species involved during the CO_2 reduction process in the eutectic (62%:38%) $LiKCO_3$. Among the different melts presently under investigation to operate in a MCEC, we decided to look specifically at the solvation properties in the eutectic (62% 38%) $LiKCO_3$ (simply denoted $LiKCO_3$ in the following). This binary mixture has a lower eutectic temperature (T = 761 K) than its other alkali-carbonates counterparts (T = 771 K for 42.7% 57.3% $LiKCO_3$, T = 774 K for 52% 48% $LiNaCO_3$ and T = 983 K for 56% 44% $NaKCO_3$). The first species are CO_2 itself and the corresponding pyrocarbonate ion $C_2O_5^{2-}$. Next, we study the end product of the reaction, *i.e.* CO. It has been proposed in cyclic voltametry experiments that CO can also react with CO_3^{2-} to form the oxalate anion according to Ref. [12].

$$CO + CO_3^{2-} \leftrightarrow C_2O_4^{2-}. \tag{1}$$

The chemical valence of carbon in oxalate is +III, which can then be seen as an intermediate species that can disproportionate into CO and CO_3^{2-}. Finally, a crucial parameter in the efficiency of MCFC and MCEC is the oxoacidity of the melt, which can be tuned through the cation composition. Oxoacidity is characterized by the dissociation constant K_D of CO_3^{2-}:

$$CO_3^{2-} \leftrightarrow CO_2 + O^{2-}. \tag{2}$$

We therefore studied in detail the solvation of O^{2-} in the eutectic $LiKCO_3$.

The paper is organized as follows. In section Methods we present the FPMD setup used in this study. Then we present results in section Results, first discussing the reactivity of CO_2 with CO_3^{2-} in section Reactivity, then solvation structures in section Intramolecular and intermolecular structure and finally dynamics in section Diffusion and rotation. We then conclude in section Conclusion.

Methods

We studied four different systems, each one consisting of a single molecule or anion (CO_2, $C_2O_4^{2-}$, CO or O^{2-}) solvated in the eutectic (62% 38%) $LiKCO_3$ at T = 1000 K and P = 1 atm, *i.e.* close to the operating conditions of MCFC/MCEC. In these conditions, the experimental density of molten carbonate is $\rho = 1.88$ g cm^{-3} [23] and we thus placed one solvated species (CO_2, $C_2O_4^{2-}$, CO or O^{2-}), 158 lithium atoms (159 for the system that contains O^{2-}), 96 potassium atoms (97 in the case of O^{2-}) and 127 CO_3^{2-} (126 in the case of $C_2O_4^{2-}$) in a cubic box of size $a = 22.23$ Å. Periodic boundary conditions are applied in all directions. The initial positions of the atoms were obtained from a classical molecular dynamics simulation of pure $LiKCO_3$ with a force field developed previously in our lab [16]

and which was tuned using NPT simulations to reproduce the experimental density at P = 1 atm. From a pure LiKCO$_3$ equilibrated configuration, we built the simulation box for the different solvated species: for CO and CO$_2$, we removed one CO$_3^{2-}$ anion, one lithium cation and one potassium cation, and we added the solvated molecule (CO or CO$_2$ instead); for C$_2$O$_4^{2-}$ we removed two CO$_3^{2-}$ anions, one lithium cation and one potassium cation, and we added C$_2$O$_4^{2-}$; and for O^{2-} we removed one CO$_3^{2-}$ and we added the anion O^{2-}. The electroneutrality is thus ensured for each simulation box.

The molecular dynamics (MD) simulations were run in the NVT ensemble, using a velocity-Verlet integrator (with a timestep Δt = 0.5 fs) and a canonical sampling/velocity rescaling (CSVR) thermostat [24] (with τ_{CSVR} = 1 ps). The length of trajectories for CO$_2$, C$_2$O$_4^{2-}$, CO, O^{2-} is 89 ps, 60 ps, 41 ps and 43 ps, respectively. Positions of all atoms are stored at every time step for analysis.

As we aim to study the reactivity and stability of the different solvated molecules in the molten carbonate, we opted for first-principles molecular dynamics where energies and forces are calculated at each time step at a DFT level. We used the software CP2K that employs a hybrid Gaussian plane-wave method (GPW) [25–27]. To reduce the number of explicit electrons, core electrons were replaced by Goedecker-Teter-Hutter (GTH) norm-conserving pseudo-potentials [28–30]. The remaining valence electrons were projected into a double-zeta valence plus polarisation (DZVP) basis set optimized for molecules for each atom type (C, O, Li and K) [31]. A cutoff of 700 Ry was used for the electronic density. We chose the BLYP functional to determine the exchange-correlation interactions [32,33] and the DFT-D3 scheme with a cut-off of 40 Å for the dispersive interactions corrections [34]. This combination of BLYP functional and DFT-D3 correction of dispersive interactions was shown to efficiently reproduce the equation of state of different pure molten carbonate (see Ref. [14,19,20]).

We complemented these simulations with four simulations of the isolated species CO$_2$, C$_2$O$_5^{2-}$, C$_2$O$_4^{2-}$ and CO at T = 1000 K. Each of these isolated species simulations consisted of one molecule in a cubic box of size a = 22.23 Å with periodic boundary conditions, and was run for 20 ps. All parameters for the isolated species simulations (integrator, thermostat, DFT calculations, basis set and pseudopotentials) are the same as for the liquid-phase simulations. For the isolated anions (C$_2$O$_5^{2-}$, C$_2$O$_4^{2-}$), a uniformly background with charge +2 is added in the simulation box to ensure the electroneutrality.

Results

Reactivity

We first investigate the stability and the potential reactivity of CO$_2$, C$_2$O$_5^{2-}$, C$_2$O$_4^{2-}$, CO, and O^{2-} when they are present in the molten carbonate medium. Different reactions involving these molecules have been suggested in the literature based on indirect experimental evidence (*e.g.* the presence of peaks

in cylic voltammetry experiments [12]), in particular the following reactions with the carbonate anion:

$$CO_2 + CO_3^{2-} \rightarrow C_2O_5^{2-}, \tag{3}$$

$$CO + CO_3^{2-} \rightarrow C_2O_4^{2-}, \tag{4}$$

$$CO_3^{2-} \rightarrow O^{2-} + CO_2. \tag{5}$$

We thus wanted to determine whether such reactions occur in our first-principles MD simulations, but molecules are not intrinsically defined in this kind of simulations. Among different possible criteria to define the molecules from first-principles MD trajectories (*i.e.* the position of all atoms at a given time), we decided to rely on a simple hysteresis geometrical criterion: a pair of atoms (C–O or C–C) are connected at time t if their interatomic distance is below 1.7 Å or if they were connected at the previous timestep $t - \Delta t$ and their interatomic distance is still below 1.9 Å. These criteria mean that a bond can form only when the interatomic distance is below 1.7 Å and can break only when the interatomic distance becomes larger than 1.9 Å. The 1.7 Å/1.9 Å values were chosen because the radial distribution function of the C–O pair in the bulk LiKCO$_3$ is close to zero between those distances [16]. The hysterias approach allows a smoother behaviour than using only a single criterion and were inspired by the criteria used to define hydrogen bonds in water [35]. Based on these criteria, we built at each time step a $N_{atoms} \times N_{atoms}$ connectivity matrix $\mathbb{C}(t)$, with $\mathbb{C}_{ij}(t) = 1$ if atoms i and j are connected at time t and $\mathbb{C}_{ij}(t) = 0$ otherwise. We then determined the connected components of connectivity matrix $\mathbb{C}(t)$, each of these connected components is a molecule present at time t.

By applying this molecule-search analysis to the four MD trajectories, we found that: (i) the CO$_2$ molecule reacts with a carbonate to form a pyrocarbonate anion C$_2$O$_5^{2-}$ (a detailed analysis of this reaction will be given in the next paragraph), (ii) the carbon monoxide CO does not react with carbonate anions to form an oxalate during the 41 ps simulation, while the oxalate C$_2$O$_4^{2-}$ does not dissociate into CO and CO$_3^{2-}$ during the 60 ps of simulation, and (iii) similarly, none of the 507 CO$_3^{2-}$ from the four simulation boxes dissociates into O^{2-} and CO$_2$ among the 233 ps accumulated from the four simulations, while the anion O^{2-} remains stable for 41 ps of simulation. The stability of these different solvated species will allow us to present their intra- and intermolecular structure and their dynamical properties in section Intramolecular and intermolecular structure and Diffusion and rotation, respectively. In the case of the isolated species (CO$_2$, C$_2$O$_5^{2-}$, C$_2$O$_4^{2-}$, CO), we applied the same methodology and found that they are stable for the 20 ps simulation.

The formation of C$_2$O$_5^{2-}$ was already observed in CaCO$_3$ at geological condition (high pressure and high temperature T = 1773 K) [15], but the present work shows that such a reactivity exists also in the milder conditions of an operating MCFC or MCEC (atmospheric pressure, intermediate temperature T = 1000 K). Fig. 1(a) illustrates the presence of C$_2$O$_5^{2-}$ in the eutectic LiKCO$_3$. The kinetics of the formation/dissociation equilibrium of the pyrocarbonate anion affect the diffusion and the electrochemical properties of CO$_2$ solvated

in this molten carbonate and the process of MCFC and MCEC. From the MD trajectory, we quantified the stability of $C_2O_5^{2-}$ and Fig. 1(b) shows the cumulative lifetime distribution of both CO_2 and $C_2O_5^{2-}$. The lifetime of the transient $C_2O_5^{2-}$ is at maximum half an order of magnitude shorter than that of CO_2 (2.5 ps vs 12 ps). To extract the characteristic lifetime, both distributions were fitted with an exponential function and we obtained $\tau_{CO_2} = 2.3$ ps and $\tau_{C_2O_5^{2-}} = 0.6$ ps. These lifetimes are of the same order of magnitude as the one calculated in the geological $CaCO_3$ (0.88 ps for CO_2 and 0.38 ps for $C_2O_5^{2-}$), but the slower kinetics are consistent with the lower temperature. On average, the pyrocarbonate is present about $f_{C_2O_5^{2-}} = 19\%$ of the time, which means that, even as a transient species, it impacts quantitatively the thermodynamics of the solvated CO_2 (e.g. its solubility and its redox potential). From the fraction of time of presence of the pyrocarbonate $f_{C_2O_5^{2-}}$, we estimated the free enthalpy of its formation (eq. (3)), $\Delta G = RT\ln(1 - f_{C_2O_5^{2-}})/f_{C_2O_5^{2-}} = 12$ kJ.mol^{-1}. The fraction of time of presence and the free enthalpy of formation are similar as in $CaCO_3$ at 1773 K: 0.24% and 16.8 kJ mol^{-1}, respectively. We also estimated the enthalpy of formation by considering the difference of average potential energy in presence of pyrocarbonate and in presence of CO_2, $\Delta H = \langle U \rangle_{C_2O_5^{2-}} - \langle U \rangle_{CO_2} = 45$ kJ.mol^{-1}, where the bracket $\langle \cdot \rangle_I$ indicates an average over configurations where the species I is present. The reaction (3) is thus endothermic, meaning the fraction of pyrocarbonate will increase at higher temperature. The entropy of formation, $\Delta S = (\Delta H - \Delta G)/T = 33$ J.mol^{-1}, is positive, which indicates the formation of pyrocarbonate is entropically *favoured*. This latter observation seems counterintuitive as the reaction 3 reduced the number of molecules from 2 to 1, i.e. a decrease in the translational entropy. In section carbon dioxide and Pyrocarbonate anion, $C_2O_5^{2-}$, we will analyse the solvation of CO_2 and $C_2O_5^{2-}$ and show that

the solvation structure of the latter is more disordered, which may explain the positive entropy of formation.

Intramolecular and intermolecular structure

We now explore the interactions between the solvated species and the molten carbonate, in particular to understand their differences in stability and reactivity. We consider the intramolecular structure (distances, angles and dihedral angles) as well as the intermolecular solvation structures.

Carbon dioxide

We first focus on the properties of CO_2, the key molecule in the redox processes occurring within MCFC and MCEC. From the first-principles MD simulations of CO_2 solvated in $LiKCO_3$ and CO_2 isolated, we extracted the geometrical properties that characterized the CO_2 molecule: the C—O distance and the $\widehat{OCO}$ angle. Table 1 gathers the average value and the standard deviation obtained in both phases at T = 1000 K. The average C—O distance and standard deviation are identical in $LiKCO_3$ and isolated (1.18 Å and 0.03 Å, respectively). If the average and standard deviation of the $\widehat{OCO}$ angle are also similar for CO_2 solvated in $LiKCO_3$ and isolated, the full distribution (shown in Fig. 2(b)) are markedly different between the two phases. The distribution of CO_2 solvated in $LiKCO_3$ is broader than for an isolated CO_2 molecule, with a long-tail ($\widehat{OCO} < 140°$) that displays an exponential-like decay, while the full distribution for the isolated molecule coincides almost with a Gaussian curve. Fig. 2(a) illustrates a bended configuration of CO_2 solvated in $LiKCO_3$ while Fig. 2(c) shows a perfectly linear configuration of CO_2. If we had previously noticed a broader distribution of $\widehat{OCO}$ in the case of a CO_2 molecule solvated in $CaCO_3$ at T = 1773 K compared to the isolated molecule distribution at the same temperature, the $\widehat{OCO}$ distribution in $CaCO_3$ coincides however with a Gaussian
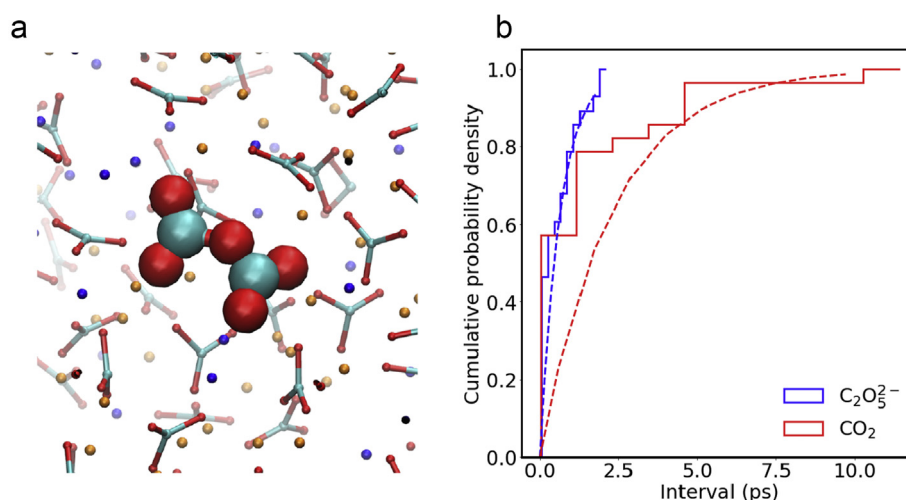

Fig. 1 — Formation/dissociation of pyrocarbonate $C_2O_5^{2-}$. (a) Snapshot of $C_2O_5^{2-}$ formed in the eutectic $LiKCO_3$. Carbonate molecules in the solvent are represented by cyan/red sticks, O atoms by red spheres, K atoms in blue and Li atoms in orange. (b) Cumulative lifetime distribution of CO_2 and of $C_2O_5^{2-}$ and exponential fit of these distributions (dashed lines). (For interpretation of the references to color in this figure legend, the reader is referred to the Web version of this article.)

Table 1 – Geometry of the different molecules in the eutectic LiKCO₃ and for an isolated species at T = 1000 K. Mean and standard deviation are obtained from the distribution of the geometrical properties (distance and angle) extracted from the MD simulations. The central atom of the $C_2O_5^{2-}$ is labelled O*.

| Molecule	Geometrical properties	in LiKCO₃		isolated species	
		Mean	Standard deviation	Mean	Standard deviation
CO_2	d_{CO} (Å)	1.18	0.03	1.18	0.03
	$\widehat{OCO}$ (°)	167.0	7.9	170.3	5.8
$C_2O_5^{2-}$	d_{CO} (Å)	1.26	0.05	1.27	0.04
	d_{CC} (Å)	2.56	0.13	2.65	0.11
	d_{CO^*} (Å)	1.49	0.11	1.51	0.09
	$\widehat{OCO}$ (°)	130.1	6.6	129.8	4.7
	$\widehat{OCO^*}$ (°)	114.5	6.3	114.7	5.7
	$\widehat{CO^*C}$ (°)	119.2	8.7	123.4	6.8
$C_2O_4^{2-}$	d_{CO} (Å)	1.28	0.05	1.29	0.04
	d_{CC} (Å)	1.57	0.08	1.65	0.09
	$\widehat{OCO}$ (°)	125.4	5.1	125.3	5.1
	$\widehat{OCC}$ (°)	116.8	6.0	117.1	5.9
CO	d_{CO} (Å)	1.16	0.06	1.15	0.02
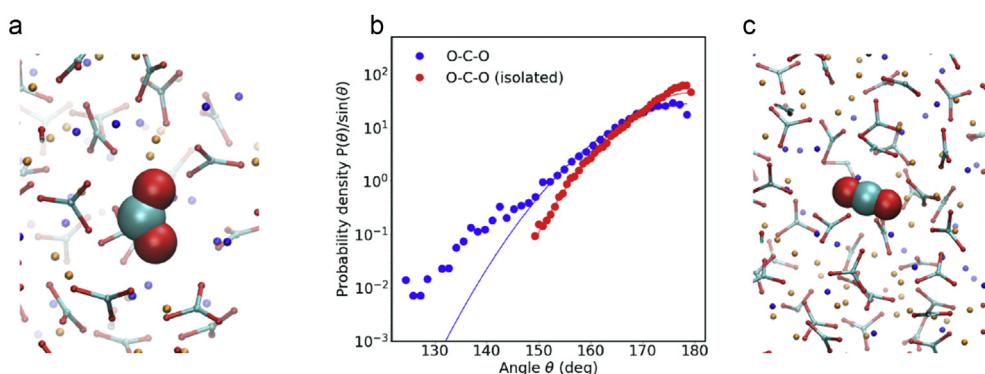
Fig. 2 – Intramolecular properties of CO₂ molecule. (a,c) Snapshots of CO₂ solvated in LiKCO₃ illustrating (a) a bended configuration ($\widehat{OCO}$ = 124.4°) and (c) a linear configuration ($\widehat{OCO}$ = 179.9°). (b) Distribution of O−C−O angle of the CO₂ molecule solvated in the eutectic LiKCO₃ at 1000 K and isolated. For the solvated molecule, angles are measured during the time intervals of existence of CO₂. The distribution is normalized by dividing by $\sin\theta$. Gaussian fits of the form $\exp(A(\theta − 180°)^2 + B)$ are shown as blue and red solid lines for the solvated molecule and isolated molecule cases. Values of the fitted parameters: A = −0.0045, B = 3.33 (solvated molecule) and A = −0.0067, B = 3.81 (isolated molecule). (For interpretation of the references to color in this figure legend, the reader is referred to the Web version of this article.)

curve, even at small angles ($\widehat{OCO} < 140°$). In both LiKCO₃ and CaCO₃, these large $\widehat{OCO}$ distributions indicate that the CO₂ molecules can bend up to 120°, facilitating the formation of the pyrocarbonate. The larger distribution in LiKCO₃ implies the CO₂ bending is more likely in this molten carbonate rather than in CaCO₃, but the difference of temperature between the two systems (1000 K in LiKCO₃ and 1773 K in CaCO₃) prevents us from discussing further the (small) difference of lifetime of CO₂ (2.3 ps in LiKCO₃ and 0.88 ps in CaCO₃).

To understand better the formation of the pyrocarbonate, we explored the solvation structure around CO₂ and its specific interactions with the different ions of the melt. Fig. 3 displays the radial distribution function (RDF) between (a) the carbon atom (C_{CO_2}) and (b) the oxygen atoms (O_{CO_2}) and all the solvent atoms (K, Li and C and O atoms of the carbonate, denoted respectively C_{carb} and O_{carb}). The potassium cations

show the strongest affinity with the CO₂ molecule, with a clear intermolecular structure characterized by two peaks, at 4 Å and 6.5 Å for C_{CO_2} and 3.5 Å and 7 Å for O_{CO_2}. The situation is notably different for the lithium cations, for which we observed no peaks in the RDF with C_{CO_2} or O_{CO_2}, meaning that no specific interaction exists between CO₂ and lithium. This absence of interaction may be explained by the competition with the strong lithium-carbonate interactions. The latter is revealed in the RDFs for C_{carb}-Li and O_{carb}-Li pairs shown in the Fig. 4 of Ref. [16]. The O_{carb}-Li RDF displays in particular a very strong peak at 2.5 Å. The neutral CO₂ molecule cannot interact strongly enough with Li⁺ to counteract the CO_3^{2-}-Li⁺ interaction and Li does not form a solvation structure around CO₂.

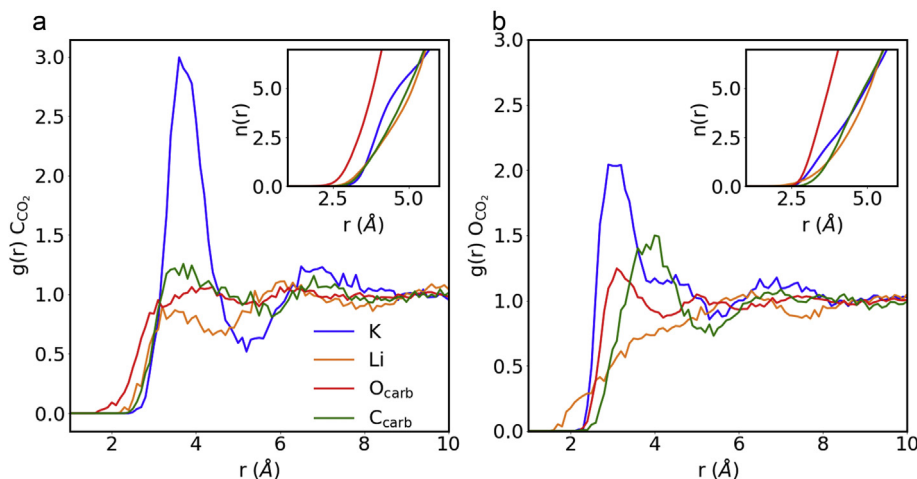The RDFs give only access to isotropic information and therefore neglect the particular orientation of the CO₂ with

Fig. 3 – Radial distribution function (RDF) around the (a) oxygen atom of CO_2 molecule O_{CO_2} and (b) carbon atom of CO_2 molecule C_{CO_2}. Intermolecular distances are measured during the time of existence of CO_2 as a molecular species. Insets: coordination number $n(r)$ obtained from the integration of the radial distribution functions. The same color code applies for figures (a) and (b). (For interpretation of the references to color in this figure legend, the reader is referred to the Web version of this article.)

respect to the carbonate, potassium and lithium ions. To better highlight the three-dimensional solvation structure of CO_2, we built two-dimensional histograms of the probability of the presence of the solvent atoms (C_{carb}, O_{carb}, Li and K) around CO_2 in a cylindrical $\rho - \zeta$ coordinate system, where ζ is the projection of an atom position along the O_{CO_2}-O_{CO_2} axis and ρ the distance from the O_{CO_2}-O_{CO_2} axis. The origin of the cylindrical coordinate system is chosen to be the mid-point of the O_{CO_2}-O_{CO_2} vector, *i.e.* close to the average position of C_{CO_2}. Fig. 4(a–d) shows these two-dimensional histograms for C_{carb}, O_{carb}, Li and K atoms, respectively.

Fig. 4(a and b) reveals a preferential orientation of CO_3^{2-} with respect to CO_2. The highest probability of presence is observed in the region $3 < \rho < 4$ Å and $-1 < \zeta < 1$ Å for C_{carb} and in the region $2.5 < \rho < 3.5$ Å and $-0.5 < \zeta < 0.5$ Å for O_{carb}. The solvation of the CO_2 molecule by the carbonate anion is thus characterized by a preferential structure where one O of the solvating carbonate is in the plane of symmetry orthogonal to CO_2. Such a preferential orientation was previously observed for CO_2 solvated in the molten $CaCO_3$ and participates to the formation of the pyrocarbonate. The solvation structure of K^+ around CO_2 is also anisotropic, as shown in Fig. 4(d). The presence of K^+ is the highest within two regions, which are symmetrical with respect to the $\zeta = 0$ axis, which have the shape of an arc of circle with center C_{CO_2} and a radius of 4 Å (that corresponds to the first peak in the RDF between K and C_{CO_2}) and which extend between the angles 46° and 65° with respect to the $\zeta = 0$ axis (maximum around 56°). The potassium cation positions preferentially between the carbon and the oxygen atoms and close to the CO_2 molecule. The two-dimensional histogram has thus permitted to analyse in details the first peak of the K-C_{CO_2} RDF. Such a double-arc structure in-between C and O atoms was also observed in the case of the probability of presence of Ca atoms around CO_2 in $CaCO_3$, which indicates that K^+ and Ca^{2+} play similar role in

the solvation of CO_2. On the other hand, the lithium solvation structure (displayed in Fig. 4(c)) does not show any preferred positions for lithium around CO_2, which confirms the previous analysis of the Li-C_{CO_2} RDF and corroborates the absence of specific Li–CO_2 interaction, probably due to the strong Li^+-CO_3^{2-} interaction. The observation of the different solvation structures formed by Li and K around CO_2 is a major step to understand the role of the molten carbonate composition in the solubility or diffusivity of CO_2.

Pyrocarbonate anion, $C_2O_5^{2-}$

We will now consider the structure and the solvation of the unusual pyrocarbonate cation formed by reaction between the solvated CO_2 molecule and a carbonate CO_3^{2-} of the solvent. We first calculated the average and standard deviation of the intramolecular distances, both for a pyrocarbonate solvated within the molten carbonate and isolated. The central oxygen atom of $C_2O_5^{2-}$ will be labelled O* while the four external oxygens and the two carbons will be labelled O and C. Table 1 gathers these distances, that follow on average the trend $\langle d_{CO} \rangle < \langle d_{CO^*} \rangle < \langle d_{CC} \rangle$ and whose standard deviations due to thermal fluctuations are relatively low (between 4% and 7%). The distances d_{CO} and d_{CO^*} are almost identical between the solvated pyrocarbonate and the isolated pyrocarbonate (with difference in average value or standard deviation < 0.02 Å), while $\langle d_{CO} \rangle$ is slightly longer for the isolated molecule, with an increase of 0.09 Å compared to the solvated anion. The average intramolecular distances of the pyrocarbonate in $LiKCO_3$ are also similar to the one in $CaCO_3$, whose average value are 1.26 Å, 1.43 Å and 2.53 Å for d_{CO}, d_{CO^*} and d_{CC}, respectively. Table 1 also displays the average and standard deviation of the three intramolecular angles of the pyrocarbonate. Like for the distances, the thermal fluctuations are of the order of 5%–7%, the average values are equivalent between the solvated and the isolated molecule
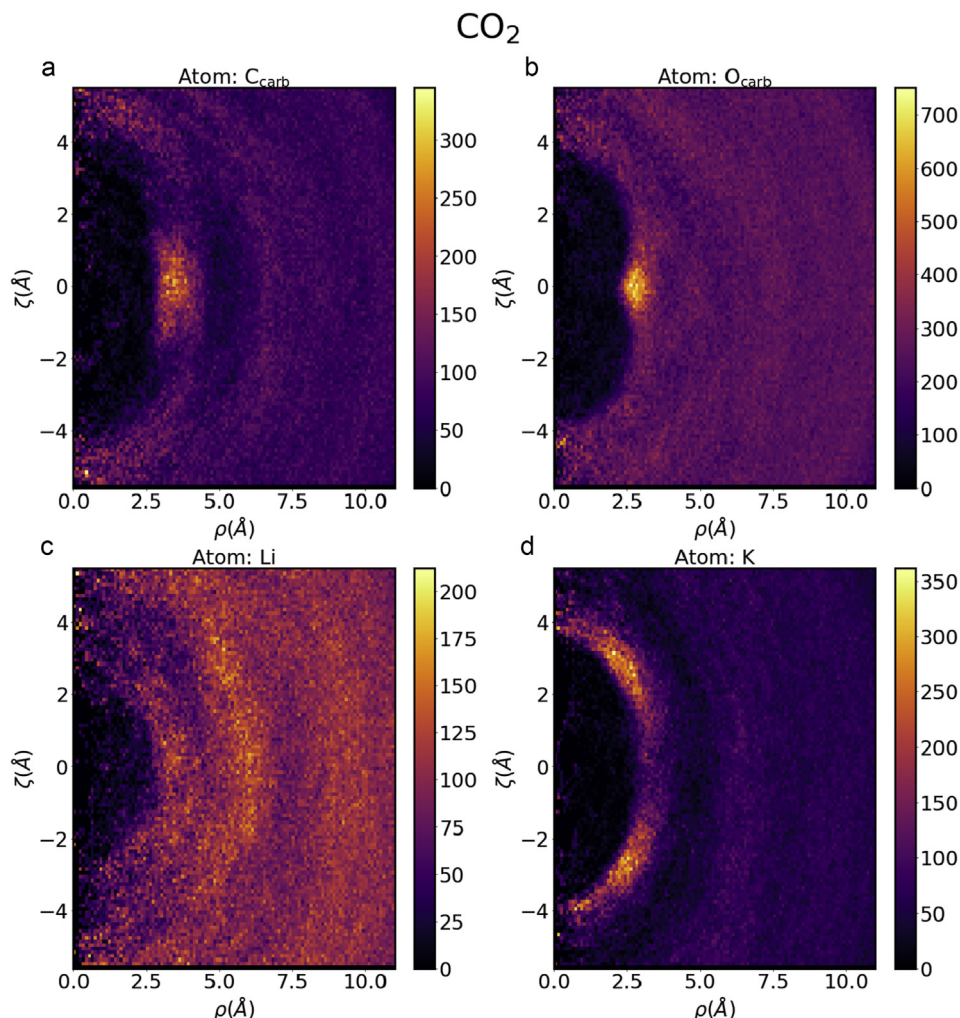
Fig. 4 — Solvation structure around the CO_2 molecule. Two dimensional colour charts representing the probability of the presence of the following atoms around CO_2: C_{carb} atom (a); O_{carb} atom (b): Li atom (c) and K atom (d). CO_2 is oriented with its O_{CO_2}-O_{CO_2} axis along the $\widehat{\zeta}$ direction, where $\zeta = 0$ is the mid-point of the O—O distance. ζ is thus the projection of an atom position along the O_{CO_2}-O_{CO_2} axis, and ρ its distance from the O_{CO_2}-O_{CO_2} axis. (For interpretation of the references to color in this figure legend, the reader is referred to the Web version of this article.)

(with the maximum difference for $\widehat{CO^*C}$ at 4.2°). They are also very close between pyrocarbonate ion solvated in $LiKCO_3$ and ion solvated in $CaCO_3$ (with the maximum difference for $\widehat{CO^*C}$ at 4.0°). Finally, we conclude the analysis of the geometry of $C_2O_5^{2-}$ by looking at the dihedral angle O—C—O*—C. Fig. 5 displays the distributions of O—C—O*—C for the solvated and isolated pyrocarbonate. Both distributions peak around 0° and 180° which indicates the pyrocarbonate forms preferentially a planar structure. The probability to observe other angles is however far from negligible: the smallest probability is found for dihedral angles of ±90° and is only half of the highest probability (planar structure). $C_2O_5^{2-}$ is therefore flexible and it alternates planar and twisted structures.

To understand the formation and relative stability of this transient species, we analyse here its solvation structure. We start with the RDF (shown in Fig. 6(a–c)), between the three types atoms of $C_2O_5^{2-}$ (C_{pyro}, O_{pyro} and O_{pyro}^*, respectively) and the four solvent atoms (C_{carb}, O_{carb}, Li and K). The RDFs reveal a different structure of solvation compared to the CO_2 molecule: the closest peak (i.e. intramolecular distance) occur now with Li for all atoms in pyrocarbonate, with distances of 3 Å and 2 Å for C_{pyro} and O_{pyro} respectively. But except for these peaks, the lithium solvation does not present a medium-range structure (RDF close to 1 after 5 Å). The RDFs K-C_{pyro} and K-O_{pyro} are characterized by a double-peak structure, more pronounced for C_{pyro}, a behaviour similar to the one observed around CO_2. The RDFs between the carbonate atoms and C_{pyro} and O_{pyro} displays almost no solvation-induced structuration, with a small peak (RDF close to 1.3) between C_{carb} and C_{pyro} and O_{pyro} at 4 Å and 6 Å respectively, while no peaks occur for C_{carb}. We conclude the discussion of the RDFs by noting that O_{pyro}^* is embedded with the pyrocarbonate molecule and less reachable: its RDFs with solvent atoms (see Fig. 6(c)) does not present any marked solvation structure (except a broad peak for potassium).
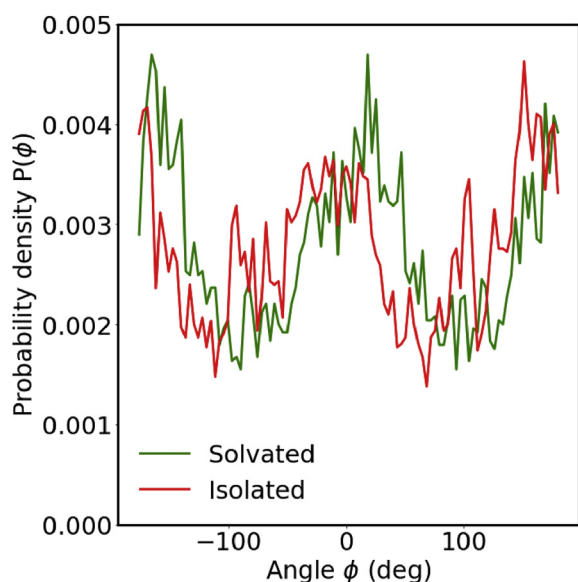
Fig. 5 – Distribution of O–C–O*–C dihedral angle of pyrocarbonate $C_2O_5^{2-}$ solvated in the eutectic LiKCO$_3$ at 1000 K and isolated. For the solvated molecule, the dihedral angle is measured during the time intervals of existence of $C_2O_5^{2-}$.

As explained in the case of CO_2, the RDFs only provide isotropic information and we therefore calculated the two-dimensional cylindrical-based histograms to characterize the solvation structure and elucidate the peaks observed in the RDFs with respect to Li and K. Fig. 6(d and e) displays the cylindrical-coordinate density of probability of presence of solvent atoms surrounding the pyrocarbonate. ζ is now the projection along the C_{pyro}-C_{pyro} axis, ρ the distance with this axis and the origin is the midpoint between C_{pyro} atoms. To account for the dissymmetry that might be induced by the formation of pyrocarbonate from the reaction between CO_2 and CO_3^{2-}, we always placed the C from the former CO_2 in the region $\zeta < 0$. Fig. 6(c) shows that the lithium atoms surround almost homogeneously the pyrocarbonate, which means the peak in RDF between lithium and pyrocarbonate does not split clearly into different preferential positions. We note nevertheless a slightly higher density of probability in the arc of circle $\zeta \geq 0$, $\rho = 3$ Å (and in particular in the place perpendicular to the pyrocarbonate, $\zeta = 0$) which reveals that the lithium cation is closer to the former CO_3^{2-} than with the former CO_2. The same analysis holds for the probability of presence of K^+ (shown in Fig. 6(d) which also surround homogeneously the pyrocarbonate but with a higher probability of presence both in the perpendicular plane but also in the C_{pyro}-C_{pyro} axis ($\rho = 0$ Å, $\zeta = \pm 4$ Å). We note that such homogeneous surrounding was also observed for the presence of calcium atoms around the pyrocarbonate formed in CaCO$_3$, which again underlines the similar role played by K^+ and Ca^{2+} in the solvation of CO_2 and $C_2O_5^{2-}$.

The cylindrical-coordinate density of probability reveals the key difference of the solvation structure around CO_2 and around $C_2O_5^{2-}$: (i) Li^+ rarely approaches close to CO_2 while it

solvates $C_2O_5^{2-}$ homogeneously at 3 Å, and (ii) K^+ solvates CO_2 anisotropically while it surrounds $C_2O_5^{2-}$ homogeneously. The difference of solvation of Li^+ may be related to the difference of charges of these molecules ($q_{CO_2} = 0, q_{pyro} = -2$), $C_2O_5^{2-}$ can compete with CO_3^{2-} to interact with the lithium cation, leading to that stronger solvation than between CO_2 and Li. The slight anisotropy of solvation of Li^+ around $C_2O_5^{2-}$ is another signature of stronger solvation of Li^+ with the former CO_3^{2-} than to the former CO_2. It indicates that the solvation structure around $C_2O_5^{2-}$ may not reach a fully equilibrated configuration (which would have been symmetrical) during the short lifetime of existence of $C_2O_5^{2-}$. The potassium plays a role in the solvation of both CO_2 and $C_2O_5^{2-}$, but it displays a more disordered structure around $C_2O_5^{2-}$. This result may contribute to the positive sign of the entropy of formation discussed in section Reactivity. When the pyrocarbonate anion is formed, the anisotropic solvation structure of K^+ around CO_2 disappears, leading to an increase of entropy.

Oxalate anion, $C_2O_4^{2-}$

Besides CO_2 and pyrocarbonate, the oxalate anion $C_2O_4^{2-}$ may also play a role in the electrochemical properties of MCFC and MCEC. The formation of this species can occur *via* the reaction between CO and CO_3^{2-} (eq. (4)), though we did not directly observe this reaction in the system containing a CO molecule or the inverse reaction in the system containing $C_2O_4^{2-}$ (see the discussion on stability in section Reactivity). From the 60 ps MD trajectory containing the stable $C_2O_4^{2-}$ solvated in LiKCO$_3$, we extracted the intramolecular and solvation structure, in particular to understand its relative stability in comparison with the pyrocarbonate.

The oxalate intramolecular geometry is characterized by two distances (d_{CC} and d_{CO}), two angles ($\widehat{OCC}$ and $\widehat{OCO}$) whose average values and standard deviations in both molten carbonate and vacuum (*i.e.* for the isolated molecule) are presented in Table 1. The shortest distance is d_{CO}, with an average value (1.28 Å) close to that of pyrocarbonate (1.26 Å) but 8% longer than in CO_2 (1.18 Å). Similarly to what we observed for CO_2 and the pyrocarbonate anion, the thermal fluctuations for the distances and the angles are small (about 5%) and solvated oxalate and isolated oxalate ions have almost identical structure (only the CC distance is 5% higher for the isolated molecule). Finally, Fig. 7(a) shows the distribution of the dihedral angle OCCO for both the solvated molecule and the isolated one. The maxima of distribution are situated at $\pm$ 100°, indicating the oxalate is preferentially twisted (as illustrated in Fig. 7(b)). Similarly to what was observed for pyrocarbonate, the distribution of dihedral angles is widely spread, the minimum is found at 0°, with a probability only half of the maximal value. Like the pyrocarbonate ion, the oxalate anion is flexible and alternates twisted and planar structures when solvated in molten carbonate.

The solvation structure of the oxalate is characterized by the RDF (Fig. 8(a and b)) and the cylindrical density of probability (Fig. 8(c and d)). The analysis of RDFs between the atoms of the oxalate (O_{oxa} and C_{oxa}) and the solvent atoms reveal some similarity with the solvation structure of pyrocarbonate,
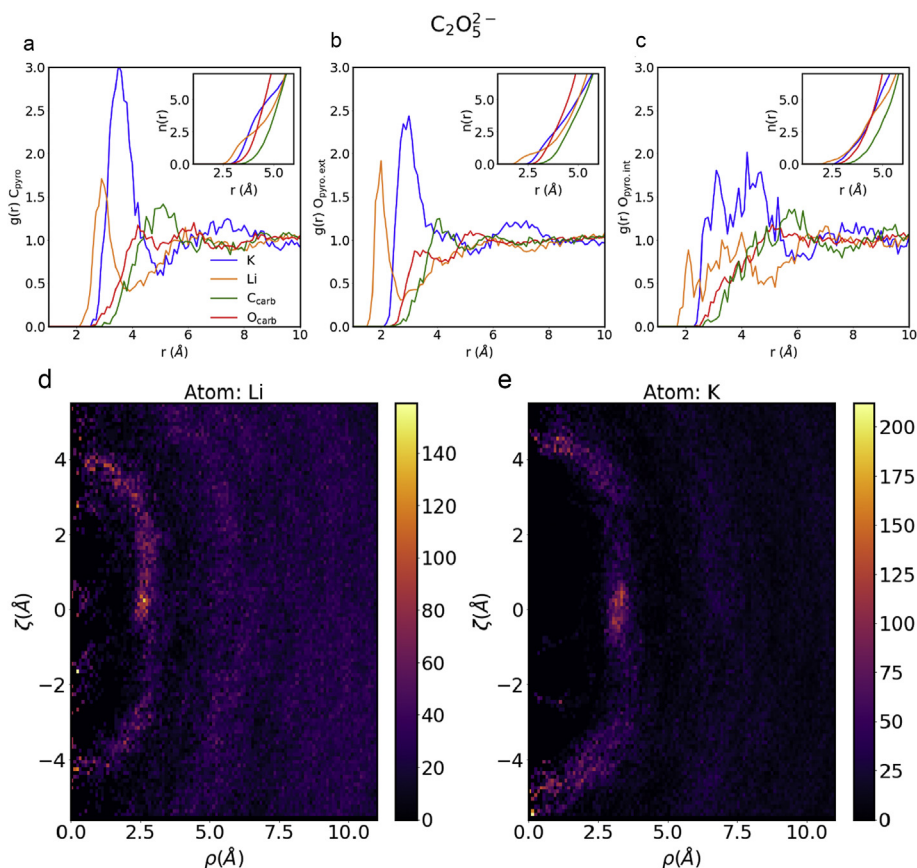
Fig. 6 – Solvation structure around the pyrocarbonate anion $C_2O_5^{2-}$. Upper panel: radial distribution function (RDF) for (a) carbon atom (b) external oxygen atoms and (c) internal oxygen atom of $C_2O_5^{2-}$. Insets: coordination number $n(r)$ obtained from the integration of the radial distribution functions. The same color code applies for figures (a), (b) and (c). Lower panel: two dimensional colour charts representing the probability of the presence of the following atoms around $C_2O_5^{2-}$: Li atom (d) and K atom (e). $C_2O_5^{2-}$ is oriented with its C_{pyro}-C_{pyro} axis along the $\hat{\zeta}$ direction, where $\zeta = 0$ is the mid-point of the C_{pyro}-C_{pyro} distance. ζ is thus the projection of an atom position along the C_{pyro}-C_{pyro} axis, and ρ its distance from the C_{pyro}-C_{pyro} axis. The C of the former CO_2 molecule is always placed in the negative ζ portion of the plots. (For interpretation of the references to color in this figure legend, the reader is referred to the Web version of this article.)

both being anionic species: (i) the RDFs with lithium peak closer than the RDFs with potassium, with a larger Li-O_{oxa} RDF peak than K-C_{oxa}, while Li-C_{oxa} RDF peak is smaller than K-C_{oxa} RDF peak; (ii) the RDF K-C_{oxa} exhibits a two-peak structure; (iii) the RDFs with C_{carb} and O_{carb} display only a very slight structuration, though the RDF C_{carb}-C_{oxa} presents two distinct peaks at 5 Å and 9 Å.

Likewise, the cylindrical densities of probability of presence of Li and K (Fig. 8(c and d)) show some resemblance with the one of pyrocarbonate. Here the cylindrical coordinates are defined with respect to the C_{oxa}-C_{oxa} axis, with ζ the projection onto this axis, ρ the distance to that axis and the origin the midpoint of the C_{oxa}-C_{oxa} bond. Li and K atoms surround homogeneously the oxalate, with a higher density for lithium along the C_{oxa}-C_{oxa} axis and for potassium in the plane perpendicular to the C_{oxa}-C_{oxa} axis ($\zeta = 0$ Å) and along the C_{oxa}-C_{oxa} axis. This solvation structure, close to that of $C_2O_5^{2-}$, indicates the existence of different solvation patterns between charged species (pyrocarbonate, oxalate) and neutral species (CO_2). The only minor difference between $C_2O_4^{2-}$ and $C_2O_5^{2-}$

relates to the lithium solvation structure which displays a slight asymmetry around $C_2O_5^{2-}$ but a perfect symmetry around $C_2O_4^{2-}$. As discussed in section Pyrocarbonate anion, $C_2O_5^{2-}$, this asymmetry originates from the reacting species forming $C_2O_5^{2-}$. We will confirm the differential solvation patterns between charge and neutral species by looking now into the solvated CO molecules and the oxygen anion O^{2-}.

Carbon monoxide

The production of carbon monoxide CO is one of the main objectives of molten carbonate electrolyser cells (MCEC) and we therefore present here the solvation properties of CO in the eutectic $LiKCO_3$. In particular, the stability of CO discussed in section Reactivity will be analysed by comparing the solvation structures of CO and CO_2. The dynamical properties, and in particular the diffusion, will be discussed in section Diffusion and rotation.

From the 41 ps first-principles MD simulation, we measure the average C–O distance and standard deviation in both the molten carbonate and in vacuum (*i.e.* for the isolated
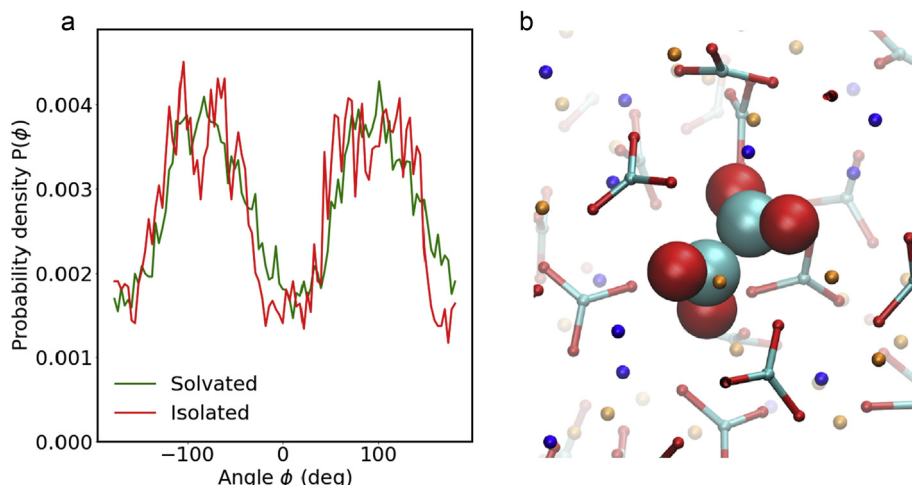
Fig. 7 — **(a) Distribution of O—C—C—O dihedral angle of oxalate $C_2O_4^{2-}$ solvated in the eutectic LiKCO3 at 1000 K and isolated. (b) Snapshot of $C_2O_4^{2-}$ in the eutectic $LiKCO_3$. Carbonate molecules in the solvent are represented by cyan/red sticks, O atoms by red spheres, K atoms in blue and Li atoms in orange. (For interpretation of the references to color in this figure legend, the reader is referred to the Web version of this article.)**

molecule). The average C—O distance is similar in molten carbonate and for the isolated molecule and is the smallest C—O intramolecular distance among the different solvated molecules we investigated (it is 0.02, 0.10 and 0.12 Å smaller than C—O distance in CO_2, pyrocarbonate and oxalate, respectively), as expected due to its triple-bond nature. The thermal fluctuations are of the order of 5% in the molten carbonate and 3% for the isolated molecule.

More interestingly, the solvation around CO is notable for its absence of marked structure. Fig. 9(a and b) shows the RDFs between the two atoms of CO (panel a for O_{CO} and panel b for C_{CO}) and the different solvent atoms. These RDFs present some similarity with the ones around CO_2. First, the highest peak is between potassium and C_{CO} and panel O_{CO} at 3.5 Å and 4 Å, respectively, with a second smaller peak observed between C_{CO} and K at 6.5 Å. The first C_{CO}—K RDF peak reaches however a value of 2 for CO and 3 for CO_2, that indicates a weaker interaction in the case of CO. Secondly, the RDFs with Li reveal an absence of preferential CO—Li distance, similar to that was already noticed for CO_2. Finally, the RDFs with the carbonate atoms show a slight solvation structure around O_{CO}: the RDF O_{carb}-O_{CO} peaks at 3.5 Å (with a value of 1.4), while the RDF O_{CO}-C_{carb} peaks at 4 Å (with a value of 1.5). As no peaks are observed for C_{CO} in Fig. 9(b), this shows that the carbonate anion surrounds preferentially the oxygen atom of CO, with one oxygen of CO_3^{2-} pointing toward O_{CO}. This specific interaction is explained by the positive charge carried by the O atom of CO (while C carries the opposite negative charge).

This particular dipole of CO also impacts the cylindrical-coordinate density of probability for Li and K displayed in Fig. 9(c-d). Here the ζ coordinate is the projection onto the C_{CO}—O_{CO} axis, ρ is the distance to that axis, and the origin of the referential is the midpoint of the C_{CO}—O_{CO} vector. The oxygen O_{CO} is placed in the $\zeta < 0$ portion of the plots. As seen in the RDF, the probability of presence of Li is more diffuse than

the one of K, but both Li and K show their highest probability of presence in the vicinity of C_{CO}, along the C_{CO}—O_{CO} axis ($\rho = 0$ Å, $\zeta = 3$ Å), i.e. the cations of the molten carbonate position preferentially close to the negatively charged C_{CO}.

Overall, CO presents a similar solvation pattern to CO_2 with a strong solvation with K^+ and an (almost) absence of solvation with Li^+. The main differences are (i) the preferential position of Li^+ close to C_{CO}, which is explained by the negatively charged carbon that can (slightly) compete with the Li^+-CO_3^{2-} interaction, (ii) the absence of anisotropic potassium solvation structure around CO and (iii) the absence of preferential solvation of carbonate around CO.

Oxygen anion

We conclude our analysis of solvated species in the molten carbonate $LiKCO_3$ with the oxygen anion O^{2-}. O^{2-} may be involved in the electrochemical processes at the interface between molten carbonate and electrodes in MCFC or MCEC. Moreover, in that liquid melt, it also plays the important role of being the strongest oxo-base, an analogue of OH^- in water. For this mono-atomic species, the solvation structure is isotropic and thus simply characterized by the RDFs with the different solvent atoms, shown in Fig. 10(a). The Li^+-O^{2-} RDF displays the most notable feature, with a high peak at 2 Å (RDF reaches here a value of 17) followed by a minimum (RDF close to 0) at 3 Å. This peak induces a plateau is the coordination number $n(r)$ between 2 and 3 Å at $n(r) = 4$, which means that O^{2-} forms a relatively stable solvation shell with four lithium atoms. Besides the O^{2-}-Li^+ RDF peak, each RDF between O^{2-} and the other solvent atoms displays successively a much smaller peak (RDF is around 2) at 3, 3.5 and 4 Å for K, O_{carb} and C_{carb}, respectively.

To prolong the RDFs analysis, we calculate the joint probability of presence of Li^+ and K^+ in the first solvation shell of O^{2-} (Li^+ and K^+ are included in the shell if their distance with O^{2-} is below the first minimum in the respective RDFs, i.e.

$$C_2O_4^{2-}$$

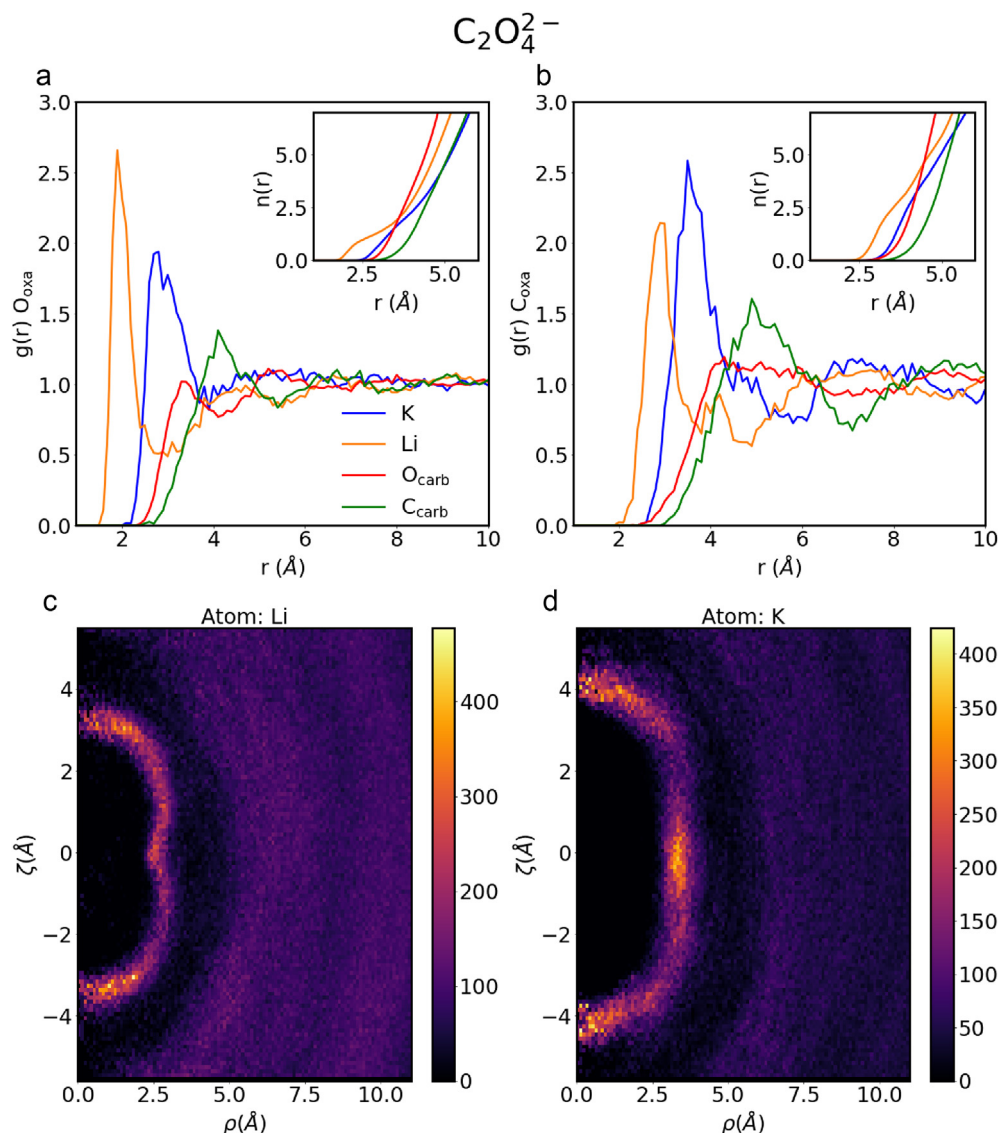Fig. 8 – Solvation structure around the oxalate $C_2O_4^{2-}$ anion. Upper panel: radial distribution function (RDF) for (a) carbon atom of $C_2O_4^{2-}$ and (b) oxygen atom of $C_2O_4^{2-}$. Insets: coordination number $n(r)$ obtained from the integration of the radial distribution functions. The same color code applies for figures (a) and (b). Lower panel: two dimensional colour charts representing the probability of the presence of the following atoms around $C_2O_4^{2-}$: Li atom (c) and K atom (d). $C_2O_4^{2-}$ is oriented with its C_{oxa}-C_{oxa} axis along the $\widehat{\zeta}$ direction, where $\zeta = 0$ is the mid-point of the C_{oxa}-C_{oxa} distance. ζ is thus the projection of an atom position along the C_{oxa}-C_{oxa} axis, and ρ its distance from the C_{oxa}-C_{oxa} axis. (For interpretation of the references to color in this figure legend, the reader is referred to the Web version of this article.)

3.1 Å and 3.6 Å respectively). This joint probability, displayed in Fig. 10(b), shows that the first shell contains most likely four Li^+ and no K^+, but structures with only three Li^+, only five Li^+ or one K^+ and three Li^+ are also significant. Cumulative distribution of residence times for both cations are shown in Fig. 10(c) together with an exponential fit of the long-time tails of the distribution (we disregard the short timescales related to vibrational motions). These distributions reveal different timescales: Li^+ stays on average 8 ps around O^{2-}, as given by the exponential decay, and up to tens of ps for some ions. On the opposite, the presence of K^+ is more short-lived with an

exponential decay time of 1.5 ps. From the RDFs, the coordination number, the joint distribution and the residence time, a picture emerges of a transient complex OLi_4^{2+} with fast entrance/exit of K^+. We explore the internal structure of this complex by looking at the distribution of Li–O–Li, Li–O–K and K–O–K angles (shown in Fig. 10(d)). These angles distributions peak around 90° and 180° with minima around 125° and the ratio between the highest and lowest probability is only a factor 2. These results indicate that (i) tetrahedral configurations are not predominant and (ii) the structure of the complex is flexible with many configurations possible. To summarize
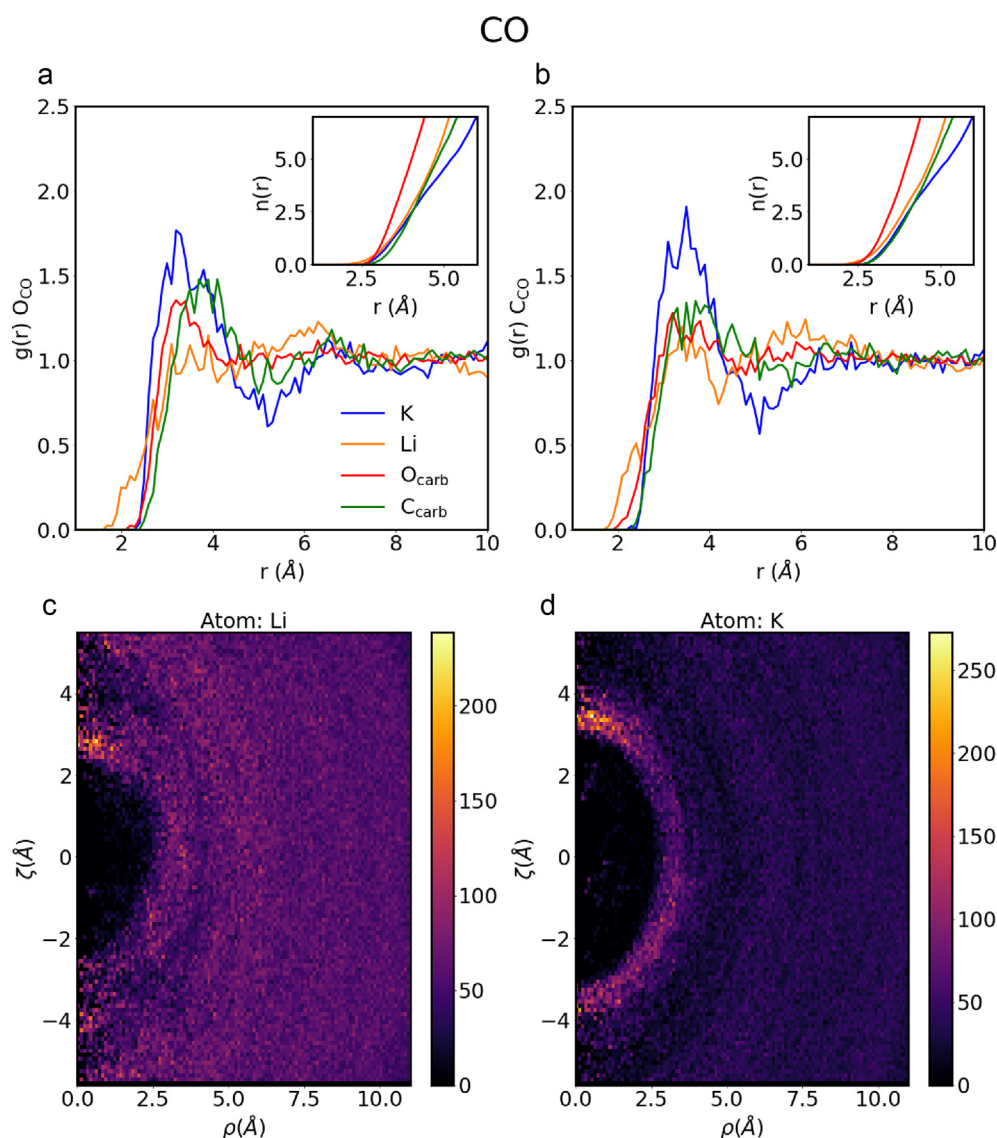
Fig. 9 – **Solvation structure around the carbon monoxide CO. Upper panel: radial distribution function (RDF) for (a) carbon atom of CO and (b) oxygen atom of CO. Insets: coordination number $n(r)$ obtained from the integration of the radial distribution functions. The same color code applies for figures (a) and (b). Lower panel: two dimensional colour charts representing the probability of the presence of the following atoms around CO: Li atom (c) and K atom (d). CO is oriented with its $O_{CO}-C_{CO}$ axis along the $\widehat{\zeta}$ direction, where $\zeta = 0$ is the mid-point of the $O_{CO}-C_{CO}$ distance and O_{CO} is always placed in the negative ζ portion of the plots. (For interpretation of the references to color in this figure legend, the reader is referred to the Web version of this article.)**

our analysis of the solvation of O^{2-}, we have shown the existence of a transient complex OLi_4^{2+} of electrochemical relevance, rather than the isolated O^{2-} anion. This complex displays a flexible structure, easily distorted by the fast entrance/exit of K^+ within the first solvation shell.

Diffusion and rotation

We now conclude the analysis of these solvated species in $LiKCO_3$ by investigating two dynamical properties: the translational diffusion in the liquid and the reorientation of these molecules.

The diffusion of these species within the molten carbonate medium —to and from the electrodes— is an essential step in the electrochemical processes of MCFC/MCEC, but the values of diffusion coefficient are often difficult to obtain experimentally. In MD simulations, the diffusion coefficient of a given molecule is obtained by taking the slope of the mean-square displacement (MSD) at long time, $D_I = \lim_{\tau \to \infty} \frac{1}{6} \frac{dMSD_I(\tau)}{d\tau}$, with $MSD_I(\tau) = \langle |\mathbf{R}_I(\tau) - \mathbf{R}_I(0)|^2 \rangle$ and where $\mathbf{R}_I(t)$ is the center-of-mass of molecule I at time t and the bracket represents an average over time. We applied this MSD definition for $C_2O_4^{2-}$, CO, O^{2-} as well as the solvent molecules, but we must take a special care in the case of the reactive CO_2.
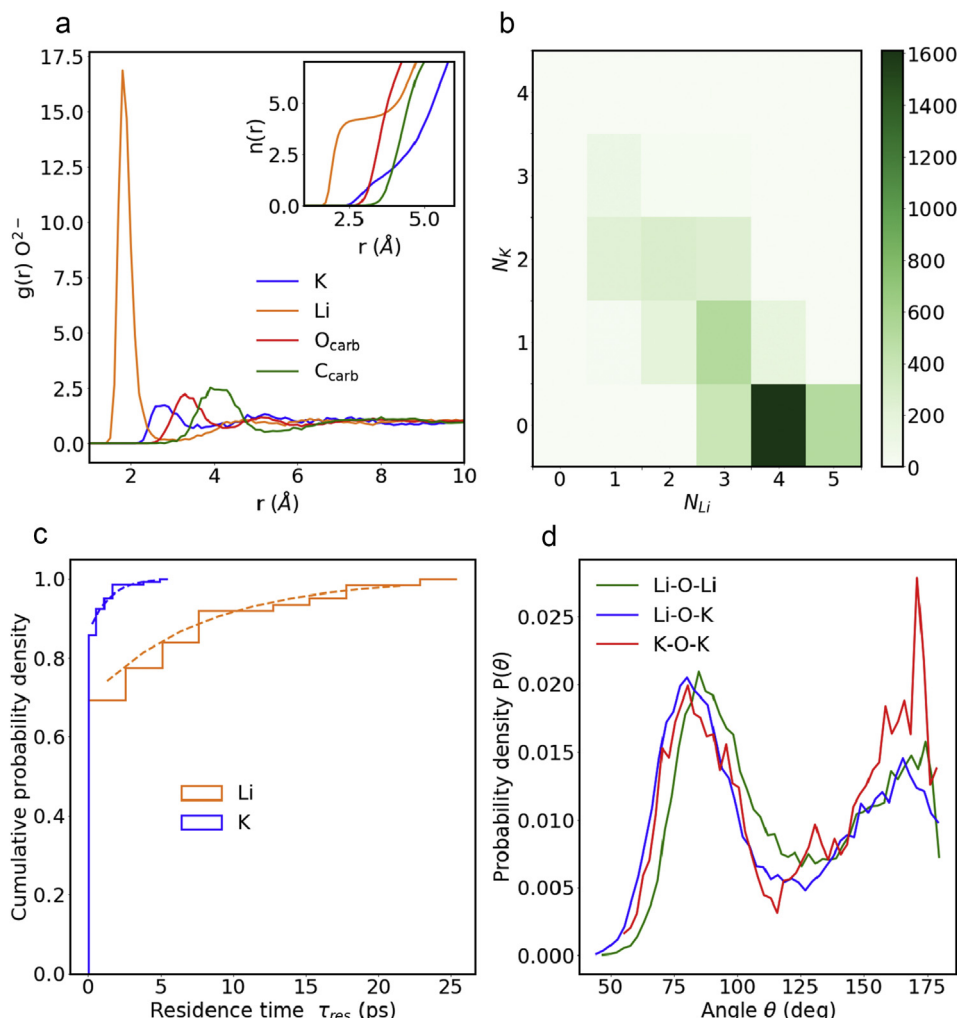
Fig. 10 — (a) Radial distribution function (RDF) for oxygen anion O^{2-}. Insets: coordination number $n(r)$ obtained from the integration of the radial distribution functions. (b) Distribution of the joint probability of presence of lithium and potassium cations within the first solvation shell of (defined with distance O—Li < 3.1 Å and distance O—K < 3.6 Å). (c) Cumulative residence time τ_{res} distribution of lithium and potassium cations and exponential fit for the long-tail of these distributions (dashed lines). (d) Distribution of X—O—X angle (where X stands for lithium or potassium cations) within the first solvation shell of O^{2-}. The distribution is normalized by dividing by $\sin\theta$.

We adapt the definition of the MSD to integrate the transient nature of CO_2 and the variable index of its constituent atoms,

$$\text{MSD}_{CO_2}(\tau) = \frac{\sum_{t=1}^{N_{steps}}|\mathbf{R}(t+\tau)-\mathbf{R}(t)|^2 \chi_t \chi_{t+\tau}}{\sum_{t=1}^{N_{steps}} \chi_t \chi_{t+\tau}} \qquad (6)$$

where the characteristic function $\chi_t = 1$ if CO_2 is present at time t and $\chi_t = 0$ otherwise. Fig. 11(a) shows the MSDs vs time for the four solvated species and the linear functions fitted on the MSDs to extract the diffusion coefficients. The latter are summarized in Table 2 together with the diffusion coefficient for the three ionic species that composed the solvent. The diffusion coefficient range from 0.5 to $4 \cdot 10^{-5}$ cm^2.s^{-1}, where the highest diffusion coefficient is found for CO. We explain this feature of CO by noting that CO is a neutral molecule, with a small electrostatic dipole ($p_{CO} = 0.11$ D), a relatively small size and a near spherical shape. These features indicates that CO interacts only weakly with the surrounding molten

carbonate and behaves probably similarly to a noble gas that can diffuse quickly in the liquid. The second highest diffusion coefficient is that of the CO_2 species. The MSD for CO_2 (eq. (6)) takes into account its reactivity and the displacement induced by the successive formation and dissociation of pyrocarbonate. If CO_2 shares some similarity with CO (a neutral molecule with a small dipole moment), its interaction with the solvent is stronger, in particular with the carbonate anion CO_3^{2-} that forms a preferential structure as discussed in section Carbon dioxide. The smallest diffusion coefficient is that of the oxygen anion O^{2-} ($0.54 \cdot 10^{-5}$ cm^2.s^{-1}). As described in section Oxygen anion, this divalent anion strongly attracts four lithium ions to form a relatively stable OLi_4^{2+} complex that could explain its slow diffusivity due its larger size and bulkier nature. We also note that the diffusion coefficient of the solvent molecules are three times smaller than the one measured experimentally at 1100 K [36] ($3.52 \cdot 10^{-5}$ cm^2 for
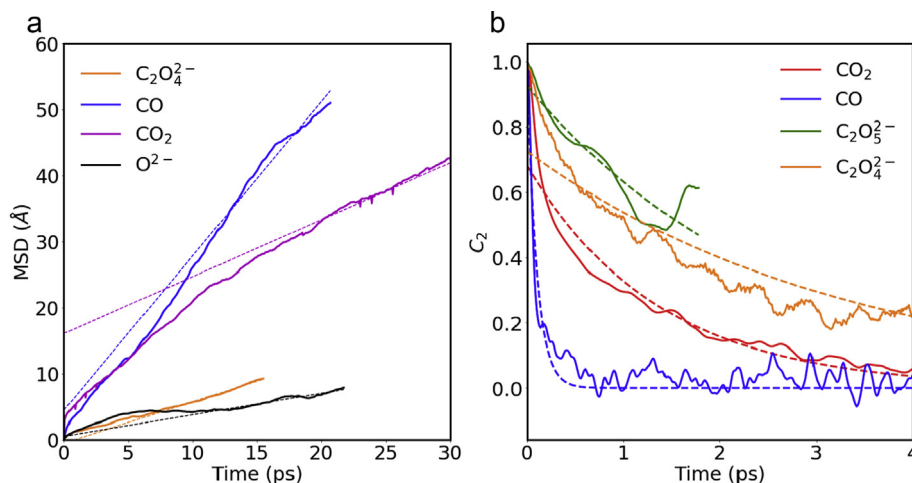
Fig. 11 – Dynamical properties of the solvated species. (a) Mean-square displacement (MSD) along time. The MSD are fitted to a linear function (dashed lines) to calculate the diffusion coefficient, see Table 2. The MSD for CO_2 molecule is calculated between times where the CO_2 molecule is present. (b) Reorientation time-correlation functions $C_2(t)$ (eq. (8)). The $C_2(t)$ function are fitted to an exponential decay function to determine the reorientation time, see Table 2.

Table 2 – Dynamical properties of the molecules solvated in the eutectic LiKCO₃. The diffusion coefficient is obtained from a linear fitting of the mean-square displacement, and the reorientation time from an exponential fitting of the time-correlation reorientation function (eq. (8)).

Molecule	Diffusion coefficient (10^{-5} cm².s⁻¹)	Reorientation time (ps)
CO_2	1.4	1.4
$C_2O_5^{2-}$	–	2.6
$C_2O_4^{2-}$	1.0	3.4
CO	3.9	0.1
O^{2-}	0.54	–
CO_3^{2-}	0.69	1.3
Li^+	2.4	–
K^+	1.4	–

CO_3^{2-} and $3.81 \cdot 10^{-5}$ cm² for K^+), but they correspond to the calculated diffusion coefficient from MD simulations in the 1100 K–1200 K temperature range [16,37–39] (0.55–1.9 · 10^{-5} cm², 2.55–5.38 · 10^{-5} cm² and 1.55–4.99 · 10^{-5} cm² for CO_3^{2-}, Li^+ and K^+ respectively).

We then analysed our simulations to obtain information on the reorientation of these species in the molten carbonate, a property that could be more easily measured experimentally and may bring information on their diffusion mechanism. We quantified the reorientation process in our MD simulations using the second-order reorientation time-correlation function.

$$C_2(t) = \langle P_2[\mathbf{u}(t) \cdot \mathbf{u}(0)]\rangle \tag{7}$$

$$= \langle \frac{1}{2}\left(3|\mathbf{u}(t)\cdot\mathbf{u}(0)|^2 - 1\right)\rangle \tag{8}$$

where P_2 is the second-order Legendre polynomial and $\mathbf{u}$ is a normalized vector characterizing the orientation of the

molecule (we choose the vector between O atoms for CO_2, between C atoms for $C_2O_5^{2-}$ and $C_2O_4^{2-}$ and between C and O atoms for CO). Fig. 11(b) shows the reorientation time-correlations $C_2(t)$ for the different solvated molecules, as well as an exponential-fitted decay (of the form $A\exp(-t/\tau_{reor})$) of $C_2(t)$. The reorientation times obtained from the fit, τ_{reor}, are gathered in Table 2 for the different solvated molecules and for the solvent anion CO_3^{2-}. Except for the particular case of CO molecule ($\tau_{reor} = 0.1$ ps), the reorientation times range between 1.3 ps and 3.4 ps with the following order: $CO_3^{2-} < CO_2 < C_2O_4^{2-} < C_2O_5^{2-}$. The short reorientation time of the CO molecule indicates that it can freely rotate in the molten carbonate and confirms the observation made for the translational diffusion that CO only weakly interacts with the molten carbonate. In contrast, the oxalate and pyrocarbonate anions are charged and relatively large molecules whose reorientation is about 30 times slower than CO.

Conclusion

We have investigated in this work the solvation properties of key molecules in the operation of MCFC/MCEC in the eutectic (62% 38%) LiKCO₃ using first-principles molecular dynamics. Similar to what happens in molten CaCO₃, we find that the solubilized CO_2 molecule spontaneously reacts with CO_3^{2-} to form the transient pyrocarbonate species $C_2O_5^{2-}$. The lifetime of the pyrocarbonate anion is however significantly longer in the eutectic LiKCO₃ than in CaCO₃, possibly because of the lower temperature. In contrast to $CO_2/C_2O_5^{2-}$, both CO and the oxalate anion, $C_2O_4^{2-}$, are found to be stable in the eutectic LiKCO₃. This confirms the oxalate anion as a putative intermediate in the reduction of CO_2. Its disproportionation reaction (or inversely its formation) is probably activated as it needs not only the breaking of the C–C bond but also the breaking and formation of a C–O bond. Such activated process are unlikely to be observed during the simulation times

accessible to our first-principles simulations, and further studies are needed to describe the formation mechanism and thermodynamics of oxalate. Free energy methods could be employed in combination with first-principles molecular dynamics in order to measure these thermodynamics properties.

The study of the solvation structures highlights the different behaviour of K^+ and Li^+ in the molten carbonate medium. Because of its smaller size, Li^+ binds more strongly to charged species ($C_2O_5^{2-}$, $C_2O_4^{2-}$, O^{2-} and CO_3^{2-}). O^{2-} forms in particular a flexible complex with four Li^+. K^+ is found preferentially around neutral molecules (CO_2 and CO). These contrasting behaviour regarding solvation between Li^+ and K^+ — and their effects on solubility and transport properties — may contribute to the choice of an optimal molten carbonate composition to operate an MCEC process.

Finally, we have estimated the diffusion coefficients of these solvated species, which are important parameters for the interpretation of experimental data and the modelling of MCEC operation. Of all the species studied, CO diffuses significantly faster consistently with its small size and poor interaction with the melt. In the future, we plan to compute other experimental observables allowing for a direct comparison with in situ experiments, such as Raman spectra or NMR chemical shifts [40].

Declaration of competing interest

The authors declare that they have no known competing financial interests or personal relationships that could have appeared to influence the work reported in this paper.

Acknowledgements

REFERENCES

[1] Frangini S, Massi A. Molten carbonates for advanced and sustainable energy applications: Part II. Review of recent literature. Int J Hydrogen Energy 2016;41(42):18971—94. https://doi.org/10.1016/j.ijhydene.2016.08.076.

[2] Cassir M, McPhail S, Moreno A. Strategies and new developments in the field of molten carbonates and high-temperature fuel cells in the carbon cycle. Int J Hydrogen Energy 2012;37(24):19345—50. https://doi.org/10.1016/j.ijhydene.2011.11.006.

[3] Campanari S, Chiesa P, Manzolini G. CO_2 capture from combined cycles integrated with Molten Carbonate Fuel Cells. International Journal of Greenhouse Gas Control 2010;4(3):441—51. https://doi.org/10.1016/j.ijggc.2009.11.007.

[4] Chery D, Lair V, Cassir M. Overview on CO_2 valorization: challenge on molten carbonate. Front. Energy Res. 2015;3(43). https://doi.org/10.3389/fenrg.2015.00043.

[5] Mastropasqua L, Pierangelo L, Spinelli M, Romano MC, Campanari S, Consonni S. Molten Carbonate Fuel Cells retrofits for CO_2 capture and enhanced energy production in the steel industry. International Journal of Greenhouse Gas Control 2019;88:195—208. https://doi.org/10.1016/j.ijggc.2019.05.033.

[6] Hu L, Rexed I, Lindbergh G, Lagergren C. Electrochemical performance of reversible molten carbonate fuel cells. Int J Hydrogen Energy 2014;39(23):12323—9. https://doi.org/10.1016/j.ijhydene.2014.02.144.

[7] Chery D, Albin V, Lair V, Cassir M. Thermodynamic and experimental approach of electrochemical reduction of CO_2 in molten carbonates. Int J Hydrogen Energy 2014;39(23):12330—9. https://doi.org/10.1016/j.ijhydene.2014.03.113.

[8] Chery D, Lair V, Cassir M. CO_2 electrochemical reduction into CO and C in molten carbonates: a thermodynamic point of view. Electrochim Acta 2015;160(43):74—81. https://doi.org/10.1016/j.electacta.2015.01.216.

[9] Hu L, Lindbergh G, Lagergren C. Electrode kinetics of the NiO porous electrode for oxygen production in the molten carbonate electrolysis cell (MCEC). Faraday Discuss 2015;182:493—550. https://doi.org/10.1039/c5fd00011d.

[10] Hu L, Lindbergh G, Lagergren C. Performance and durability of the molten carbonate electrolysis cell and the reversible molten carbonate fuel cell. J Phys Chem C 2016;120(25):13427—33. https://doi.org/10.1021/acs.jpcc.6b04417.

[11] Kaplan V, Wachtel E, Gartsman K, Feldman Y, Lubomirsky I. Conversion of CO_2 to CO by electrolysis of molten lithium carbonate. J Electrochem Soc 2010;157(4):B552—6. https://doi.org/10.1149/1.3308596.

[12] Chery D, Albin V, Meléndez-Ceballos A, Lair V, Cassir M. Mechanistic approach of the electrochemical reduction of CO_2 into CO at a gold electrode in molten carbonates by cyclic voltammetry. Int J Hydrogen Energy 2016;41(41):18706—12. https://doi.org/10.1016/j.ijhydene.2016.06.094.

[13] Meskine H, Gürbüz E, Albin V, Meléndez-Ceballos A, Cassir M, Ringuedé A, Lair V. CO_2 electrolysis in a reversible molten carbonate fuels cell: online chromatographic detection of CO, Int J Hydrogen Energy 2021;46:14913—21. https://doi.org/10.1016/j.ijhydene.2020.08.028.

[14] Vuilleumier R, Seitsonen A, Sator N, Guillot B. Structure, equation of state and transport properties of molten calcium carbonate ($CaCO_3$) by atomistic simulations. Geochem Cosmochim Acta 2014;141:547—66. https://doi.org/10.1016/j.gca.2014.06.037.

[15] D. Corradini, F.-X. Coudert, R. Vuilleumier, Carbon dioxide transport in molten calcium carbonate occurs through an oxo-Grotthuss mechanism via a pyrocarbonate anion, Nat Chem. doi:10.1038/nchem.2450.

[16] Corradini D, Coudert F-X, Vuilleumier R. Insight into the Li_2CO_3-K_2CO_3 eutectic mixture from classical molecular dynamics: thermodynamics, structure, and dynamics. J Chem Phys 2016;144(10):104507. https://doi.org/10.1063/1.4943392.

[17] Wilson M, Ribeiro MCC, Wilding MC, Benmore C, Weber JKR, Alderman O, Tamalonis A, Parise JB. Structure and liquid fragility in sodium carbonate. J Phys Chem 2018;122(4):1071—6. https://doi.org/10.1021/acs.jpca.7b10712.

[18] Gutiérrez A, Garroni S, Souentie S, Cuesta-López S, Yakoumis I, Aparicio S. Theoretical study on molten alkali carbonate interfaces. Langmuir 2018;34(43):13065—76. https://doi.org/10.1021/acs.langmuir.8b02907.

[19] Desmaele E, Sator N, Vuilleumier R, Guillot B. Atomistic simulations of molten carbonates: thermodynamic and transport properties of the Li_2CO_3-Na_2CO_3-K_2CO_3 system. J Chem Phys 2019;150(9):094504. https://doi.org/10.1063/1.5082731.

[20] Desmaele E, Sator N, Vuilleumier R, Guillot B. The $MgCO_3$-$CaCO_3$-Li_2CO_3-Na_2CO_3-K_2CO_3 melts: thermodynamics and transport properties by atomistic simulations. J Chem Phys 2019;150(21):214503. https://doi.org/10.1063/1.5099015.

[21] Car R, Parrinello M. Unified approach for molecular dynamics and density-functional theory. Phys Rev Lett 1985;55(22):2471–4. https://doi.org/10.1103/PhysRevLett.55.2471.

[22] Kono Y, Kenney-Benson C, Hummer D, Ohfuji H, Park C, Shen G, et al. Ultralow viscosity of carbonate melts at high pressures. Nat Commun 2014 Oct;14(5):5091. https://doi.org/10.1038/ncomms6091.

[23] Janz G. Thermodynamic and transport properties for molten salts: correlation equations for critically evaluated density, surface tension, electrical conductance and viscosity data. J Phys Chem Ref Data 1988;17(Suppl. 2).

[24] Bussi G, Donadio D, Parrinello M. Canonical sampling through velocity rescaling. J Chem Phys 2007;126(1):014101. https://doi.org/10.1063/1.2408420.

[25] Lippert BG, Hutter J, Parrinello M. A hybrid Gaussian and plane wave density functional scheme. Mol Phys 1997;92(3):477–88. https://doi.org/10.1080/002689797170220.

[26] VandeVondele J, Krack M, Mohamed F, Parrinello M, Chassaing T, Hutter J. Quickstep: fast and accurate density functional calculations using a mixed Gaussian and plane waves approach. Comput Phys Commun 2005;167(2):103–28. https://doi.org/10.1016/j.cpc.2004.12.014.

[27] Hutter J, Iannuzzi M, Schiffmann F, VandeVondele J. CP2K: atomistic simulations of condensed matter systems. Wiley Interdisciplinary Reviews: Computational Molecular Science 2014;4(1):15–25. https://doi.org/10.1002/wcms.1159.

[28] Goedecker S, Teter M, Hutter J. Separable dual-space Gaussian pseudopotentials. Phys Rev B 1996;54(3):1703–10. https://doi.org/10.1103/PhysRevB.54.1703.

[29] Hartwigsen C, Goedecker S, Hutter J. Relativistic separable dual-space Gaussian pseudopotentials from H to Rn. Phys Rev B 1998;58(7):3641–62. https://doi.org/10.1103/PhysRevB.58.3641.

[30] Krack M. Pseudopotentials for H to Kr optimized for gradient-corrected exchange-correlation functionals. Theoretical Chemistry Accounts 2005;114(1):145–52. https://doi.org/10.1007/s00214-005-0655-y.

[31] VandeVondele J, Hutter J. Gaussian basis sets for accurate calculations on molecular systems in gas and condensed phases. J Chem Phys 2007;127(11):114105. https://doi.org/10.1063/1.2770708.

[32] Becke AD. Density-functional exchange-energy approximation with correct asymptotic behavior. Phys Rev 1988;38(6):3098–100. https://doi.org/10.1103/PhysRevA.38.3098.

[33] Lee C, Yang W, Parr RG. Development of the Colle-Salvetti correlation-energy formula into a functional of the electron density. Phys Rev B 1988;37(2):785–9. https://doi.org/10.1103/PhysRevB.37.785.

[34] Grimme S. Semiempirical GGA-type density functional constructed with a long-range dispersion correction. J Comput Chem 2006;27(15):1787–99. https://doi.org/10.1002/jcc.20495.

[35] Laage D, Hynes JT. A molecular jump mechanism of water reorientation. Science 2006;311(5762):832–5. https://doi.org/10.1126/science.1122154.

[36] Janz GJ, Bansal NP. Molten salts data: diffusion coefficients in single and multi-component salt systems. J Phys Chem Ref Data 1982;11(3):505–693. https://doi.org/10.1063/1.555665.

[37] Tissen JTWM, Janssen GJM, Eerden Pv d. Molecular dynamics simulation of binary mixtures of molten alkali carbonates. Mol Phys 1994;82(1):101–11. https://doi.org/10.1080/00268979400100084.

[38] Koishi T, Kawase S, Tamaki S, Ebisuzaki T. Computer simulation of molten Li_2CO_3-K_2CO_3 mixtures. J Phys Soc Jpn 2000;69(10):3291–6. https://doi.org/10.1143/JPSJ.69.3291.

[39] Costa MF. Molecular dynamics of molten Li_2CO_3-K_2CO_3. J Mol Liq 2008;138(1):61–8. https://doi.org/10.1016/j.molliq.2007.08.001.

[40] Morizet Y, Vuilleumier R, Paris M. A NMR and molecular dynamics study of CO2-bearing basaltic melts and glasses. Chem Geol 2015.